An XAFS study on the specific microstructure of active species in iron titanate catalyst for NH$_3$-SCR of NO$_x$

Fudong Liu [a], Kiyotaka Asakura [b,*], Pengyang Xie [c], Jianguo Wang [c], Hong He [a,**]

[a] *Research Center for Eco-Environmental Sciences, Chinese Academy of Sciences, Beijing 100085, PR China*
[b] *Catalysis Research Center, Hokkaido University, Sapporo 001-0021, Japan*
[c] *College of Chemical Engineering and Materials Science, Zhejiang University of Technology, Hangzhou 310032, PR China*

ABSTRACT

Environmental-friendly iron titanate (FeTiO$_x$) catalyst is a potential candidate for the substitution of conventional V$_2$O$_5$—WO$_3$ (MoO$_3$)/TiO$_2$ catalyst for the selective catalytic reduction of NO$_x$ with NH$_3$ (NH$_3$-SCR) for the NO$_x$ elimination from stationary and mobile sources for environmental protection. To understand in-depth the nature of active structure in this FeTiO$_x$ catalyst for further catalyst redesign and activity improvement, the study of X-ray absorption near-edge spectroscopy (XANES) and extended X-ray absorption fine-structure spectroscopy (EXAFS) combined with theoretical calculation is carefully performed. Different from the crystal structure of hematite Fe$_2$O$_3$, homogeneous edge shared Fe^{3+}—(O)$_2$—Ti^{4+} structure in FeTiO$_x$ catalyst prepared from Ti(SO$_4$)$_2$ precursor is obviously formed with crystallite phase, which shows the electronic inductive effect between Fe^{3+} and Ti^{4+} species, resulting in the high NO adsorption and oxidation ability of Fe^{3+} species and thus high catalytic activity and N$_2$ selectivity in the NH$_3$-SCR reaction. In the future study, this specific edge shared Fe^{3+}—(O)$_2$—Ti^{4+} structure can be stabilized onto certain catalyst supports with large surface area for practical use, such as the catalytic removal of NO$_x$ from flue gas and diesel engine exhaust.

1. Introduction

Selective catalytic reduction of NO$_x$ with NH$_3$ (NH$_3$-SCR) is a well-proven technique for the removal of NO$_x$ from stationary and mobile sources for environmental protection, such as coal-fired power plants and diesel engines [1]. Due to some inevitable disadvantages of the conventional and commercial SCR catalyst V$_2$O$_5$—WO$_3$ (MoO$_3$)/TiO$_2$ including the narrow operation temperature window, the low N$_2$ selectivity at high temperatures due to the formation of large amount of N$_2$O, the high conversion of SO$_2$ to SO$_3$ and the toxicity of vanadium pentoxide to eco-environment and human health, although it has been applied for several decades in industry, many researchers still make great effort to develop new, highly efficient, stable, environmental-friendly and vanadium-free NH$_3$-SCR catalysts, such as Fe/Cu/Ce-exchanged zeolites [2–9] and Fe/Cu/Mn/Ce supported-type or mixed oxide catalysts [10–21].

Several vanadium-free catalysts have already been utilized for the catalytic removal of NO$_x$ from diesel engine exhaust in recent years, such as Fe/Cu-ZSM-5 catalysts [22].

In our previous study, we have successfully developed a novel and environmental-friendly iron titanate (FeTiO$_x$) catalyst prepared by conventional co-precipitation method, which showed high NH$_3$-SCR activity, N$_2$ selectivity and H$_2$O/SO$_2$ durability in the medium temperature range (200–400 °C) [23–26]. This FeTiO$_x$ catalyst is promising to be used in the deNO$_x$ process for flue gas and diesel engine exhaust for environmental protection. We deduced that the iron titanate crystallite with specific Fe—O—Ti structure, but not aggregated Fe$_2$O$_3$ oxide particles, was the real active phase in the NH$_3$-SCR reaction. However, no direct evidence was obtained from X-ray diffraction (XRD), UV–vis diffuse reflectance spectroscopy (UV–vis DRS), transmission electron microscopy (TEM) and Raman spectroscopy *etc.* due to the poor crystallinity of this catalyst both in the bulk phase and on the surface. In order to understand in-depth the structural nature of the active phase in this FeTiO$_x$ catalyst for further catalyst redesign and activity improvement, more powerful characterization method for determining the local structure of catalytic materials should be applied, such as the X-ray absorption fine-structure spectroscopy (XAFS).

* Corresponding author at: Catalysis Research Center, Hokkaido University, 21-10 Kita, Sapporo 001-0021, Japan. Tel.: +81 11 706 9113; fax: +81 11 706 9113.
** Corresponding author at: P.O. Box 2871, 18 Shuangqing Road, Haidian District, Beijing 100085, PR China. Tel.: +86 10 62849123; fax: +86 10 62849123.
E-mail addresses: askr@cat.hokudai.ac.jp (K. Asakura), honghe@rcees.ac.cn (H. He).

In this study, using X-ray absorption near-edge spectroscopy (XANES) and extended X-ray absorption fine-structure spectroscopy (EXAFS), we confirm that a homogeneous linkaged structure of edge shared Fe^{3+} octahedra and Ti^{4+} octahedra with severe distortion is indeed formed in $FeTiO_x$ catalyst with crystallite phase. In addition, the electronic inductive effect between Fe^{3+} and Ti^{4+} species will also be verified by the experimental results combined with theoretical calculation, which is very important to enhance the NO adsorption and oxidation ability of Fe^{3+} species and thus the catalytic activity in NH_3-SCR reaction. This new finding can provide theoretical guidance for the further design and activity improvement of this NH_3-SCR catalyst, even for other Fe—Ti containing or mixed oxide catalyst systems.

2. Experimental

2.1. Catalyst preparation

The iron titanate catalysts were facilely synthesized by conventional co-precipitation method using $TiCl_4$ or $Ti(SO_4)_2$ as Ti precursor and $Fe(NO_3)_3 \cdot 9H_2O$ as Fe precursor with the molar ratio of Fe:Ti = 1:1. When using $TiCl_4$ as Ti precursor, it was firstly diluted with ice-cold distilled water in the bath of ice–water mixture avoiding intense hydrolysis to prepare a known concentration of $TiOCl_2$ solution. Because of the slow hydrolysis of $TiCl_4$ at such a low temperature, no TiO_2 precipitation occurred during the preparation process of $TiOCl_2$ solution. Then a stoichiometric amount of $Fe(NO_3)_3$ aqueous solution was added in with subsequent stirring for 1 h without the formation of any precipitation in this process, either. Afterwards, standard $NH_3 \cdot H_2O$ (25 wt.%) aqueous solution was used as precipitator until the pH rose to 10 when the Fe and Ti ions were completely co-precipitated. Without aging, the precipitate was filtrated and washed by distilled water to remove the unwanted cations and anions from precursors and precipitator, followed by desiccation in oven at 100 °C for 12 h and calcination in muffle furnace at 400 °C for 6 h in air condition. Catalyst prepared from $TiCl_4$ precursor was denoted as $FeTiO_x$—$TiCl_4$.

When using $Ti(SO_4)_2$ as Ti precursor, $TiOSO_4$ solution could be obtained more easily because the hydrolysis of $Ti(SO_4)_2$ in H_2O was much slower than that of $TiCl_4$. $Ti(SO_4)_2$ and $Fe(NO_3)_3 \cdot 9H_2O$ were firstly dissolved together with distilled water without the formation of any precipitation, and then the rest procedures were controlled exactly the same as those of $FeTiO_x$—$TiCl_4$ catalyst. Catalyst prepared from $Ti(SO_4)_2$ precursor was denoted as $FeTiO_x$—$Ti(SO_4)_2$.

We also prepared Fe_2O_3/TiO_2 supported type catalyst (Fe:Ti = 1:1 in molar ratio) using conventional impregnation method for comparison. The anatase TiO_2 support in Fe_2O_3/TiO_2 catalyst was purchased from Shanghai Huijing Co. Firstly, the calculated amount of TiO_2 support was added into an aqueous solution of $Fe(NO_3)_3 \cdot 9H_2O$. After impregnation with stirring for 1 h, the excess water was removed in a rotary evaporator at 80 °C. Then the sample was desiccated in oven at 120 °C for 12 h, followed by calcination in muffle furnace at 400 °C for 6 h in air condition.

For the preparation of reference samples, hematite Fe_2O_3 and anatase TiO_2 were self-prepared by precipitation method using $Fe(NO_3)_3 \cdot 9H_2O$ and $Ti(SO_4)_2$ as precursors, respectively, and using standard $NH_3 \cdot H_2O$ (25 wt.%) aqueous solution as precipitator. The desiccation and calcination procedures were controlled exactly the same as those of $FeTiO_x$—$TiCl_4$ and $FeTiO_x$—$Ti(SO_4)_2$ catalysts.

Finally, all the calcined samples were crushed and sieved above 200 mesh, and then diluted by flour power with appropriate molar ratios and pressed into thin disks for XANES and EXAFS measurements.

2.2. Activity test

The steady state NH_3-SCR activity over different catalysts was tested in a fixed-bed quartz tube reactor at atmospheric pressure, and the reaction conditions were controlled as follows: 500 ppm NO, 500 ppm NH_3, 5 vol.% O_2, N_2 balance; 0.6 ml catalyst, 20–40 mesh; total flow rate of 500 ml/min and gas hourly space velocity (GHSV) = 50,000 h^{-1}. The effluent gas was continuously analysed using an FTIR spectrometer (Nicolet Nexus 670) equipped with a heated, low volume multiple-path gas cell (2 m).

2.3. XAFS measurement and data analysis

The XANES and EXAFS of Fe—K and Ti—K edges were measured in a transmission mode at room temperature on BL-7C beam line, Photon Factory, Institute of Materials Structure Science, High Energy Accelerator Research Organization (IMSS-KEK), Japan. Fe foil, FeO, hematite Fe_2O_3, ilmenite $FeTiO_3$, pseudobrookite Fe_2TiO_5, Ti foil, anatase TiO_2 (self-prepared) and rutile TiO_2 were used as reference samples. The storage ring was operated at 2.5 GeV with 300 mA as an average storage current. The synchrotron radiation beam line was monochromatized with a Si (1 1 1) double crystal monochromator, and mirrors were used to eliminate higher harmonics. The incident and transmitted beam intensities were monitored using ionization chambers filled with pure N_2.

XAFS data were analysed using the REX2000 program (Rigaku Co.). XANES spectra were normalized with edge height and then taken the first-order derivatives to compare the variation of absorption edge energies. EXAFS oscillation $\chi(k)$ was extracted using spline smoothing with a Cook–Sayers criterion [27] and weighted by k^3 in order to compensate for the diminishing amplitude in high k range because of the decay of the photoelectron wave. Thereafter, the filtered k^3-weighted $\chi(k)$ was Fourier transformed into R space (k range: 2.5–15 $Å^{-1}$ for Fe—K EXAFS and 2.5–13 $Å^{-1}$ for Ti—K EXAFS) with a Hanning function window. In the curve fitting step, the possible backscattering amplitude and phase shift were calculated using FEFF8.4 code [28].

2.4. Density functional theory (DFT) calculation

The geometry optimization of the three kinds of stoichiometric TiO_2, Fe_2O_3 and Fe_2TiO_5 crystals were carried out using Dmol3 module [29,30] in Materials Studio software package. The generalized gradient approximation (GGA) with PW91 functional was used to describe the exchange-correlation (XC) effects. The double numerical plus polarization (DNP) basis set was used in the expanded electronic wave function.

The Brillouin zone using the Monkhorst–Pack scheme was sampled by $7 \times 7 \times 3$, $6 \times 6 \times 2$ and $3 \times 7 \times 3$ for TiO_2, Fe_2O_3 and Fe_2TiO_5, respectively. For all calculations, the convergence in energy and force was set to 10^{-5} eV and 2×10^{-3} eV/Å. The atomic charges were calculated using the Hirshfeld approach. The electron density difference of the investigated crystal models was also analysed.

3. Results and discussion

3.1. NH_3-SCR activity

The steady-state NH_3-SCR activity over Fe_2O_3/TiO_2, $FeTiO_x$—$TiCl_4$ and $FeTiO_x$—$Ti(SO_4)_2$ catalysts is presented in Fig. 1. As we can see, the operation temperature window of Fe_2O_3/TiO_2 is quite narrow, and the highest NO_x conversion cannot achieve 100% either. Over $FeTiO_x$—$TiCl_4$ catalyst, the SCR activity at temperatures below 300 °C is quite low, although the SCR activity at temperatures above 300 °C is similar to that over $FeTiO_x$—$Ti(SO_4)_2$ catalyst. In a broad temperature range, the
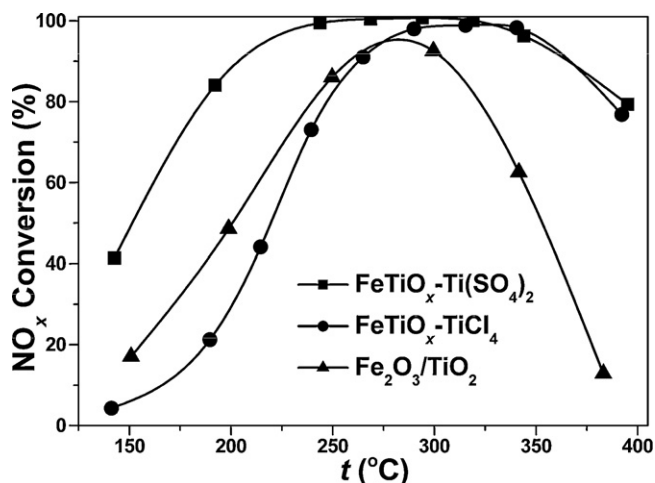
Fig. 1. Steady-state NH$_3$-SCR activity over Fe$_2$O$_3$/TiO$_2$, FeTiO$_x$—TiCl$_4$ and FeTiO$_x$—Ti(SO$_4$)$_2$ catalysts.

FeTiO$_x$—Ti(SO$_4$)$_2$ catalyst exhibits rather high deNO$_x$ efficiency, with *ca.* 90% NO$_x$ conversion obtained from 200 to 350 °C. In short summary, the NH$_3$-SCR activity over these three catalysts at low temperatures decreases in the following sequence: FeTiO$_x$—Ti(SO$_4$)$_2$ ≫ Fe$_2$O$_3$/TiO$_2$ > FeTiO$_x$—TiCl$_4$. New highly active species with specific structure should be formed in the most active FeTiO$_x$—Ti(SO$_4$)$_2$ catalyst, which will be discussed in detail in the following sections.

3.2. XANES

Fig. 2A and B shows the Fe—K XANES of reference samples, Fe$_2$O$_3$/TiO$_2$, FeTiO$_x$—TiCl$_4$, FeTiO$_x$—Ti(SO$_4$)$_2$ catalysts and their corresponding first-order derivatives, respectively. The first-order derivative peak of the absorption coefficient appears at 7122.6 eV for Fe^{2+} in FeO, while that for Fe^{3+} in pristine Fe$_2$O$_3$ appears at 7123.2 eV. Interestingly, this peak appears at 7123.4 eV in Fe$_2$TiO$_5$ reference sample, indicating the higher absorption edge energy than that of Fe$_2$O$_3$. This may be due to the electronic inductive effect by surrounding Ti^{4+} ions, in which the deviation of electron cloud occurs from Fe^{3+} to Ti^{4+} species.

As for Fe$_2$O$_3$/TiO$_2$ catalyst, the clear XANES pattern of Fe—K edge is identical with that of hematite and gives the maximum at 7123.2 eV in the first-order derivative, implying that well crystallized Fe$_2$O$_3$ exists in this catalyst.

FeTiO$_x$—Ti(SO$_4$)$_2$, the most active catalyst, gives the strongest pre-edge peak indicating the severest structure distortion probably from octahedral coordination. A peak top in the first-order derivative appears at 7123.6 eV, indicating the presence of Fe^{3+}. The higher energy of this derivative peak than that of Fe$_2$O$_3$ sample further indicates the presence of Fe^{3+}—O—Ti^{4+} linkage in this catalyst, in which the neighbouring Ti^{4+} species draws more electrons from Fe^{3+} species. This is in well accordance with our previous XPS results, in which the Fe^{3+} species on FeTiO$_x$—Ti(SO$_4$)$_2$ catalyst showed higher binding energy than that on pristine Fe$_2$O$_3$ sample [24]. The broad feature in the XANES spectrum of FeTiO$_x$—Ti(SO$_4$)$_2$ catalyst may be due to the poor crystallinity of iron titanate species with nano size effect, resulting in the less scattering of photoelectrons by neighbouring unsaturated coordination atoms, which is consistent with the
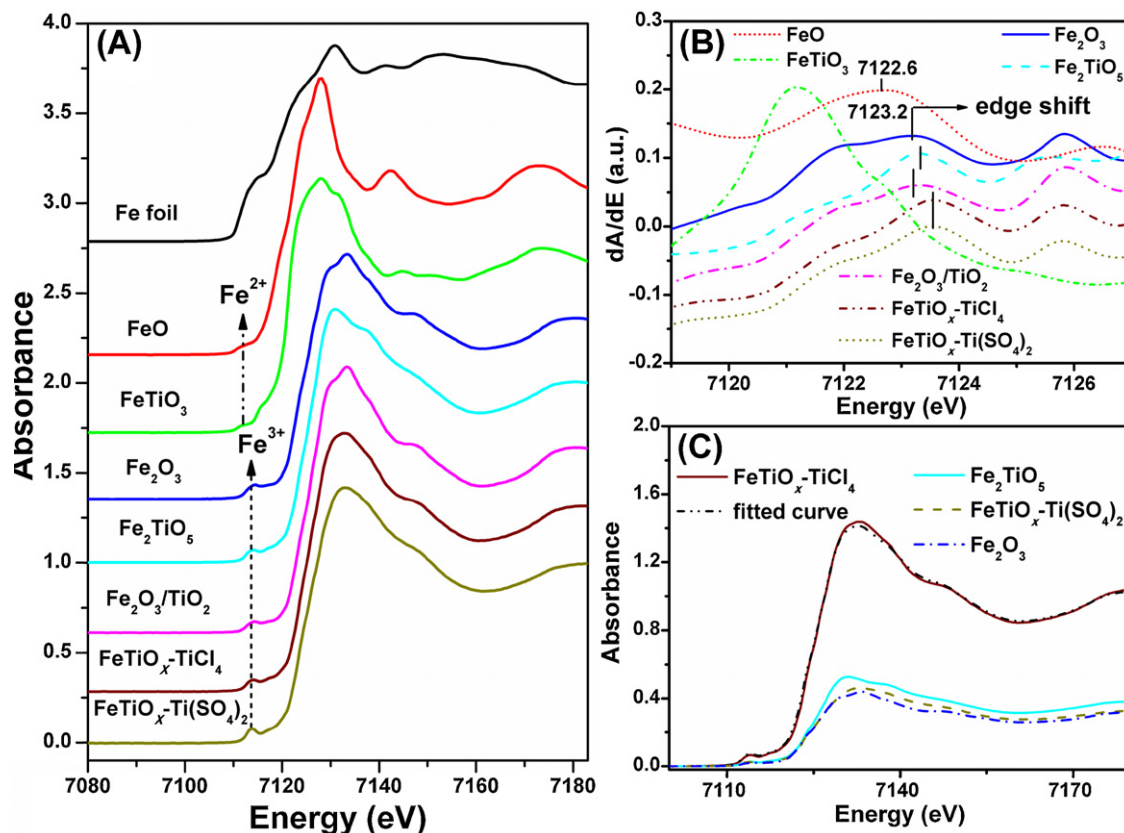

Fig. 2. (A) Fe—K XANES, (B) first-order derivatives of Fe—K XANES in different samples and (C) fitting result of Fe—K XANES in FeTiO$_x$—TiCl$_4$ catalyst using Fe$_2$TiO$_5$, Fe$_2$O$_3$ and FeTiO$_x$—Ti(SO$_4$)$_2$ as references.

rather broad XRD bumps without obvious diffraction peaks [24]. The iron titanate species may be the aggregates of small particles with specific structure, called as iron titanate crystallite. Sulfate species from $Ti(SO_4)_2$ precursor may inhibit the formation of large crystal particle in its preparation process [31]. In our previous study [32], only 0.2% S content in molar ratio from the residual sulfate species was detected on the surface of $FeTiO_x$–$Ti(SO_4)_2$ catalyst, yet this small amount of sulfate did not result in any SCR activity difference at high temperatures comparing with that of $FeTiO_x$–$TiCl_4$ catalyst (as shown in Fig. 1). As we mentioned above, the electronic field of Ti^{4+} species around Fe^{3+} species will reduce the electron density of Fe^{3+} in Fe^{3+}–O–Ti^{4+} linkage, and may facilitate the adsorption of negative molecular (such as NO with unpaired electron). This will lead to the higher NO adsorption and oxidation ability of Fe^{3+} species, as confirmed by the comparative NO_x-TPD results on Fe_2O_3 sample and $FeTiO_x$–$Ti(SO_4)_2$ catalyst in our previous study [33], which is beneficial to the promotion of low temperature NH_3-SCR activity over $FeTiO_x$–$Ti(SO_4)_2$ catalyst.
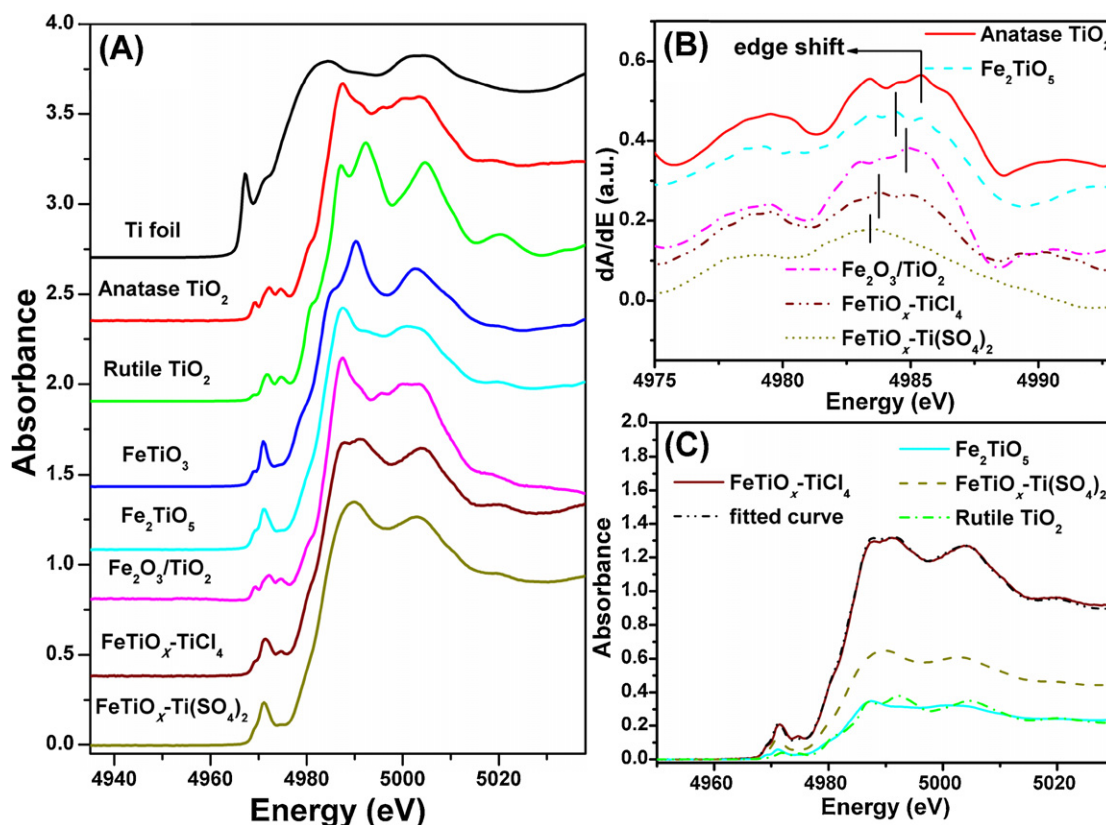
As for $FeTiO_x$–$TiCl_4$ catalyst, the first-order derivative peak of XANES appears at 7123.4 eV, also indicating the presence of Fe^{3+}. The post-edge XANES feature is similar to that of either Fe_2TiO_5 or Fe_2O_3 reference samples, but the peak is featureless. Therefore, a mixture of Fe_2TiO_5, Fe_2O_3 and iron titanate species may exist in this catalyst. Fig. 2C shows the linear fitting results of Fe–K XANES in $FeTiO_x$–$TiCl_4$ catalyst using Fe_2TiO_5, Fe_2O_3 and $FeTiO_x$–$Ti(SO_4)_2$ as reference samples, based on which we can conclude that a mixture of *ca.* 28% Fe_2TiO_5 + 23% Fe_2O_3 + 49% iron titanate species derived from $FeTiO_x$–$Ti(SO_4)_2$ existed in this catalyst (Table 1). Only half of the Fe^{3+} species in this catalyst is in the form of active iron titanate crystallite, and accordingly the low temperature NH_3-SCR activity over $FeTiO_x$–$TiCl_4$ catalyst is much lower than that over

Table 1
Linear fitting results of Fe–K and Ti–K XANES in $FeTiO_x$–$TiCl_4$ catalyst.

Sample	Fe–K XANES		Ti–K XANES	
	Reference	Ratio (%)	Reference	Ratio (%)
$FeTiO_x$–$TiCl_4$	Fe_2TiO_5	27.9	Fe_2TiO_5	25.9
	Fe_2O_3	23.3	Rutile TiO_2	25.8
	$FeTiO_x$–$Ti(SO_4)_2$	48.9	$FeTiO_x$–$Ti(SO_4)_2$	48.3

$FeTiO_x$–$Ti(SO_4)_2$ catalyst but higher than that over Fe_2O_3/TiO_2 catalyst [24].

Fig. 3A shows the Ti–K XANES of reference samples and Fe_2O_3/TiO_2, $FeTiO_x$–$TiCl_4$, $FeTiO_x$–$Ti(SO_4)_2$ catalysts. Anatase TiO_2 is the main crystal phase in Fe_2O_3/TiO_2 catalyst. Ti–K XANES of $FeTiO_x$–$Ti(SO_4)_2$ catalyst has the strongest pre-edge peak together with broad peak features in the post-edge region, indicating the presence of distorted Ti^{4+} local structure probably from octahedral coordination. XANES of $FeTiO_x$–$TiCl_4$ catalyst can be explained by a mixture of *ca.* 26% Fe_2TiO_5 + 26% rutile TiO_2 + 48% iron titanate crystallite, as shown by the linear fitting results in Fig. 3C and Table 1. It is noteworthy that the rutile TiO_2 is formed in the $FeTiO_x$–$TiCl_4$ catalyst instead of anatase TiO_2. Another interesting feature is the edge position of Ti–K edge. Fig. 3B shows the first-order derivatives of Ti–K XANES spectra. The absorption energy of Ti–K edge in Fe_2TiO_5 reference sample with the Fe^{3+}–O–Ti^{4+} linkage where both ions are located nearby is lower than that of anatase TiO_2. This can be interpreted simply by the reverse electronic inductive effect by the surrounding Fe^{3+} species, similarly to the Fe–K edge case. $FeTiO_x$–$Ti(SO_4)_2$ catalyst has the lowest absorption edge energy, indicating again the presence of most abundant Fe^{3+}–O–Ti^{4+} linkage. This phenomenon may universally exist in other Fe–Ti containing catalysts, such as Fe^{3+}-exchanged


Fig. 3. (A) Ti–K XANES, (B) first-order derivatives of Ti–K XANES in different samples and (C) fitting result of Ti–K XANES in $FeTiO_x$–$TiCl_4$ catalyst using Fe_2TiO_5, rutile TiO_2 and $FeTiO_x$–$Ti(SO_4)_2$ as references.
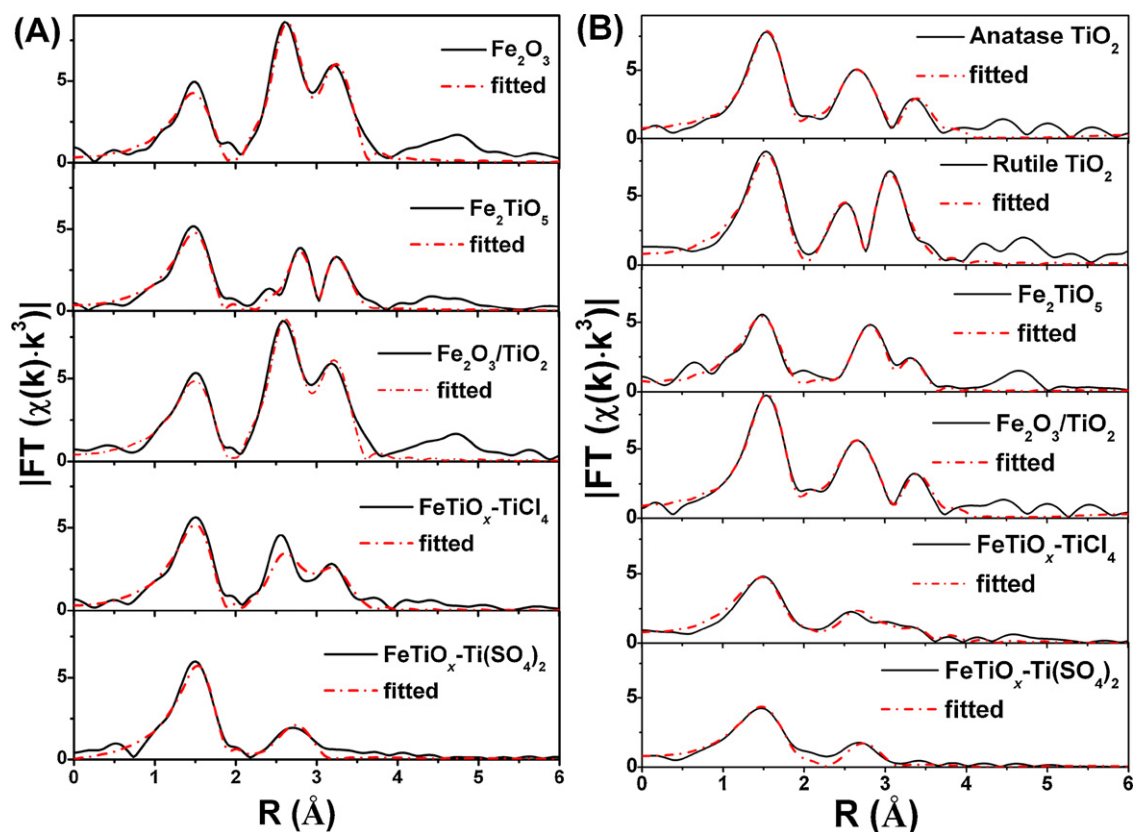
Fig. 4. Fourier transforms of filtered $k^3 \cdot \chi(k)$ into R space of (A) Fe—K and (B) Ti—K edges in different samples, where the red dashed lines correspond to the curve fitting results in R space.
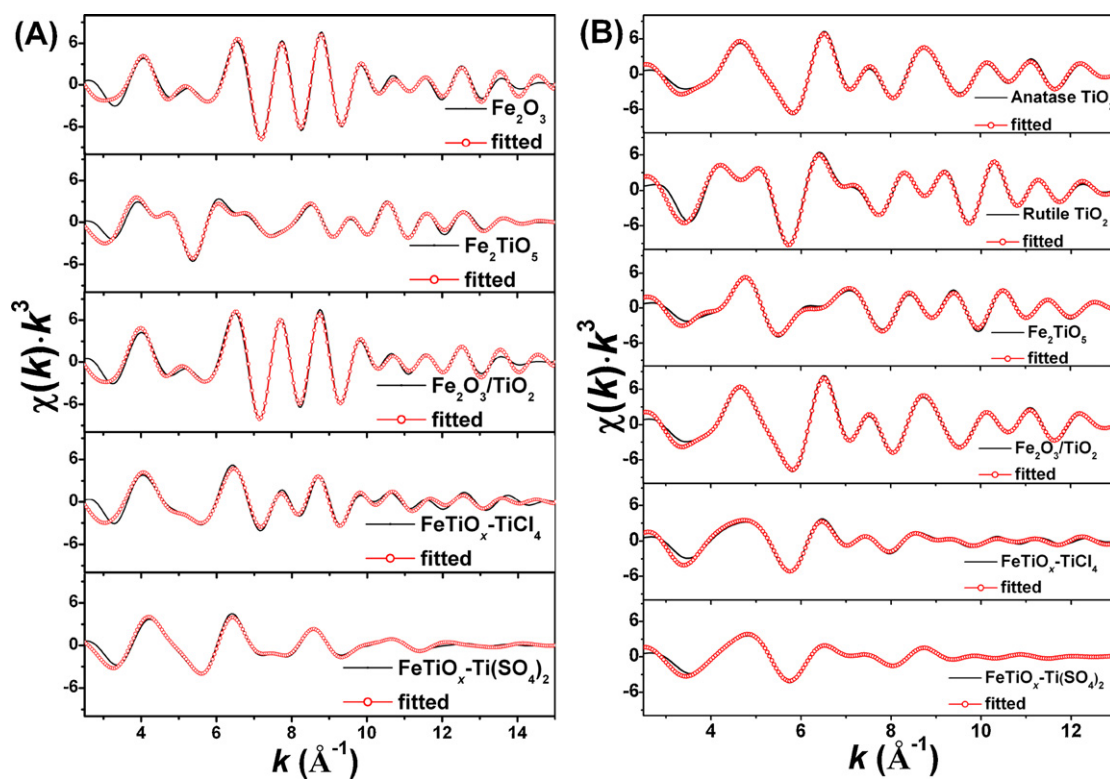
Fig. 5. Filtered $k^3 \cdot \chi(k)$ of (A) Fe—K edge in the k range of 2.5–15 Å^{-1} and (B) Ti—K edge in the k range of 2.5–13 Å^{-1} in different samples, where the red dotted lines correspond to the curve fitting results in k space.
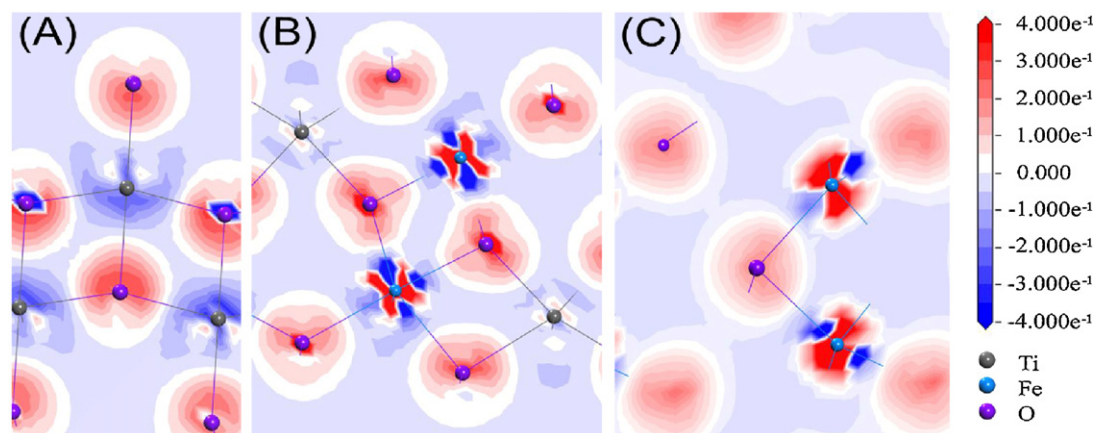
Fig. 6. Electron density differences of (A) TiO_2, (B) Fe_2TiO_5, and (C) Fe_2O_3.

TiO_2-pillared clay catalyst developed by Long and Yang [34] and Fe_2O_3/TiO_2 catalyst developed by Kato et al. [35], in which the Fe^{3+}—O—Ti^{4+} structure might also form and play important roles in the NH_3-SCR reaction.

3.3. EXAFS

Fig. 4 depicts the Fourier transform of filtered k^3-weighted EXAFS oscillations of Fe—K and Ti—K edges into R space, and all corresponding $k^3 \cdot \chi(k)$ are shown in Fig. 5. Fe_2O_3/TiO_2 catalyst has similar coordination peaks of Fe—K and Ti—K edges as those of hematite Fe_2O_3 and anatase TiO_2, respectively, which is in well accordance with the curve fitting results in Table 2 when using hematite Fe_2O_3 and anatase TiO_2 as model crystals. As suggested

by XANES results, $FeTiO_x$—$TiCl_4$ catalyst shows peaks in the second coordination shells similar to those of Fe_2TiO_5, Fe_2O_3 and rutile TiO_2. However, these peaks are much smaller due to the coexistence of iron titanate crystallite. For $FeTiO_x$—$Ti(SO_4)_2$ catalyst, the intensity of the second coordination peaks of both Fe and Ti is rather low, implying a crystallite state of this sample again. It is noteworthy that only one single peak appears for the second coordination shells of both Fe and Ti species in $FeTiO_x$—$Ti(SO_4)_2$ catalyst, which is totally different from those of reference samples and the other two catalysts.

The single peak in the second coordination shells of $FeTiO_x$—$Ti(SO_4)_2$ catalyst can be assigned to Fe^{3+}—O—Ti^{4+} linkage suggested by the XANES results. The curve fitting results in Table 2 indicate the Fe^{3+}—O—Ti^{4+} distance as 3.09 ± 0.04 Å,
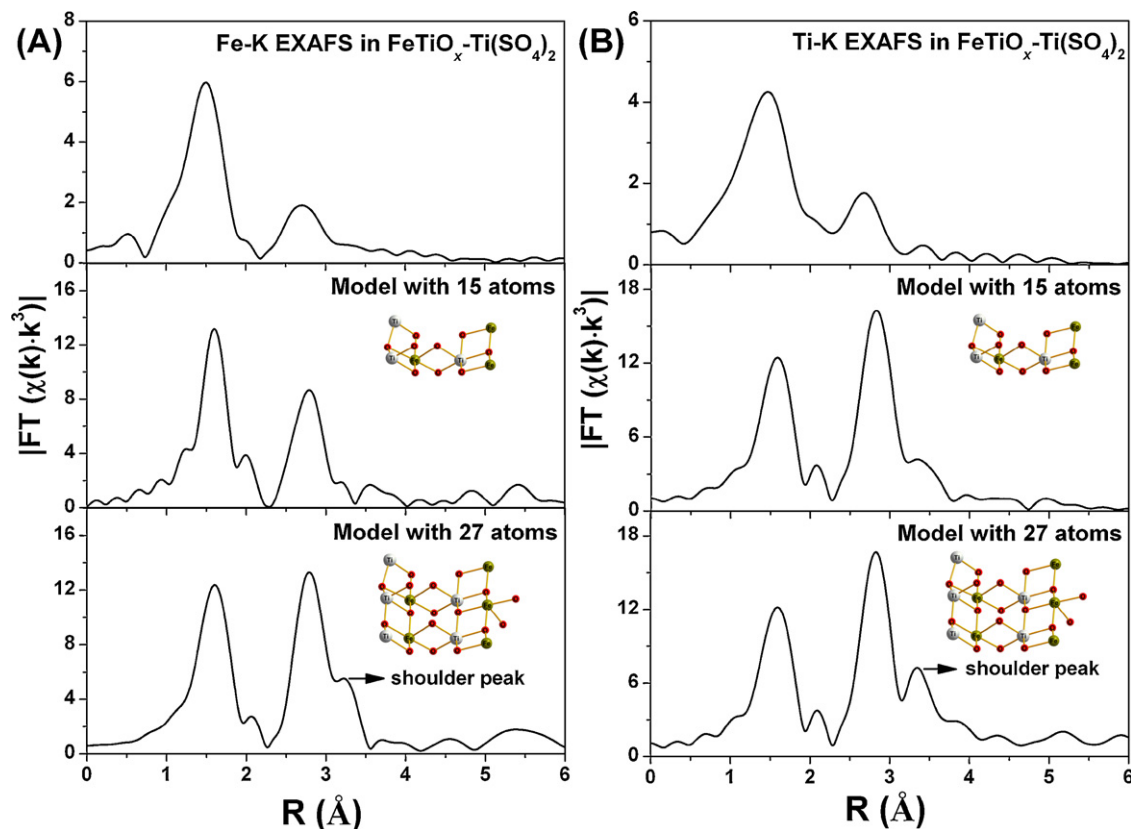

Fig. 7. Fourier transforms of filtered $k^3 \cdot \chi(k)$ (calculated by FEFF8.4 using different atom numbers in iron titanate crystallite structure) into R space of (A) Fe—K edge in the k range of 2.5–15 Å^{-1} and (B) Ti—K edge in the k range of 2.5–13 Å^{-1}.

Table 2
Curve fitting results of Fe—K and Ti—K EXAFS in different samples (corrected by the crystallographic data of Fe_2O_3, anatase TiO_2, rutile TiO_2 and Fe_2TiO_5, M = Fe or Ti).

Sample	Fe—K reference	Shell	CN[a]	R[b] (Å)	σ^{2c} (10^{-3} Å^2)	R factor (%)
Fe_2O_3	Fe_2O_3	Fe—O	6.0 ± 1.5	1.95 ± 0.03	10.2	
		Fe—Fe$_1$	3.0 ± 0.6	2.97 ± 0.02	9.0	4.2
		Fe—Fe$_2$	3.0 ± 1.0	3.36 ± 0.02	4.1	
Fe_2TiO_5	Fe_2TiO_5	Fe—O	3.0 ± 1.1	1.95 ± 0.02	7.9	
		Fe—M$_1$	3.0 ± 2.3	3.18 ± 0.04	5.2	9.0
		Fe—M$_2$	3.0 ± 2.7	3.67 ± 0.05	8.6	
Fe_2O_3/TiO_2	Fe_2O_3	Fe—O	6.6 ± 1.8	1.96 ± 0.03	9.8	
		Fe—Fe$_1$	3.4 ± 1.1	2.97 ± 0.02	10.0	3.9
		Fe—Fe$_2$	3.1 ± 1.5	3.35 ± 0.02	4.4	
$FeTiO_x$—$TiCl_4$	Fe_2TiO_5	Fe—O	6.6 ± 1.8	1.96 ± 0.02	9.0	
	*Fe_2O_3	Fe—M$_1$	1.0 ± 1.0	3.18 ± 0.04	5.2	
	§Crystallite	Fe—M$_2$	1.0 ± 2.2	3.67 ± 0.05	8.6	9.5
	Fe—O—Ti	*Fe—Fe$_1$	1.0 ± 1.4	2.97 ± 0.02	9.0	
		*Fe—Fe$_2$	1.0 ± 1.2	3.36 ± 0.02	4.1	
		§Fe—Ti	2.6 ± 2.5	3.09 ± 0.04	10.8	
$FeTiO_x$—$Ti(SO_4)_2$	Crystallite	Fe—O	7.7 ± 1.7	1.96 ± 0.01	9.0	
	Fe—O—Ti	Fe—Ti	2.6 ± 2.5	3.09 ± 0.04	10.8	4.5

Sample	Ti—K reference	Shell	CN[a]	R[b] (Å)	σ^{2c} (10^{-3} Å^2)	R factor (%)
Anatase TiO_2	Anatase TiO_2	Ti—O	6.0 ± 1.0	1.98 ± 0.01	10.2	
		Ti—Ti$_1$	3.0 ± 0.9	3.02 ± 0.02	5.9	1.7
		Ti—Ti$_2$	3.0 ± 1.6	4.03 ± 0.03	7.7	
Rutile TiO_2	Rutile TiO_2	Ti—O	6.0 ± 1.3	1.98 ± 0.02	9.2	
		Ti—Ti$_1$	2.0 ± 1.2	2.96 ± 0.04	5.0	2.9
		Ti—Ti$_2$	4.0 ± 1.4	3.57 ± 0.02	4.4	
Fe_2TiO_5	Fe_2TiO_5	Ti—O	6.0 ± 1.1	1.96 ± 0.02	11.0	
		Ti—M$_1$	3.0 ± 1.4	3.17 ± 0.03	6.7	3.3
		Ti—M$_2$	3.0 ± 2.8	3.72 ± 0.05	5.0	
Fe_2O_3/TiO_2	Anatase TiO_2	Ti—O	7.1 ± 1.8	1.98 ± 0.01	10.6	
		Ti—Ti$_1$	3.5 ± 1.5	3.02 ± 0.02	6.4	1.3
		Ti—Ti$_2$	3.5 ± 2.7	4.04 ± 0.04	8.5	
$FeTiO_x$—$TiCl_4$	Fe_2TiO_5	Ti—O	7.3 ± 1.9	1.97 ± 0.02	15.6	
	*Rutile TiO_2	Ti—M$_1$	0.9 ± 0.5	3.17 ± 0.03	6.7	
	§Crystallite	Ti—M$_2$	0.9 ± 2.5	3.72 ± 0.05	5.0	5.9
	Ti—O—Fe	*Ti—Ti$_1$	0.5 ± 0.7	2.96 ± 0.04	5.0	
		*Ti—Ti$_2$	1.0 ± 0.9	3.57 ± 0.02	4.4	
		§Ti—Fe	3.8 ± 1.7	3.08 ± 0.04	14.2	
$FeTiO_x$—$Ti(SO_4)_2$	Crystallite	Ti—O	6.9 ± 1.7	1.97 ± 0.02	15.6	
	Ti—O—Fe	Ti—Fe	2.0 ± 1.7	3.08 ± 0.04	14.2	6.9

* or §, indicates that the shells were curve fitted using Fe_2O_3/rutile TiO_2 or crystallite Fe-O-Ti/Ti-O-Fe as references, respectively.

[a] CN, coordination number.
[b] R, bond distance.
[c] σ, Debye–Waller factor.

which agrees well with the edge shared Fe—O—Ti and Ti—O—Fe structures. Compared to the edge shared Fe—O—Ti structure in well crystallized Fe_2TiO_5 reference sample, the bond distances of Fe—O—Ti and Ti—O—Fe in this catalyst is 0.09 Å shorter. This is also probably related with the nano effect of $FeTiO_x$—$Ti(SO_4)_2$ catalyst in poor crystallinity, of which the catalyst surface possesses a large proportion of unsaturated coordination atoms with shorter average bond distances. The stronger interaction between Fe^{3+} and Ti^{4+} species in this catalyst induces the shift of Fe—K absorption edge to higher energy than that of Fe_2TiO_5. Fe^{3+} species must be more positively charged on the catalyst surface and is probably responsible for its highest NH_3-SCR activity. After curve fitting, the coordination numbers of Fe—O—Ti and Ti—O—Fe bonds are 2.6 and 2.0, indicating again the small particle size or crystallite phase of iron titanate species in this catalyst.

3.4. DFT calculation

In order to further confirm the electronic inductive effect between Fe^{3+} and Ti^{4+} species in Fe—Ti containing catalyst, the DFT calculation is applied in this study based on periodical model

structures. The Hirshfeld charge of Fe in stoichiometric Fe_2O_3 and Fe_2TiO_5 is calculated to be 0.29 and 0.31, while the value of Ti in TiO_2 and Fe_2TiO_5 is calculated to be 0.57 and 0.54. In Fe_2TiO_5, the charge of Fe and Ti increases and decreases *ca.* 7 and 5% comparing with that in pristine Fe_2O_3 and pristine TiO_2, respectively. This trend can be clearly seen in the electron density difference map, as shown in Fig. 6. The electron transfers from Fe to the coordinated oxygen and further to neighbouring Ti atoms (Fig. 6B). Therefore, more charge accumulation (depletion) around Ti (Fe) can be obtained in Fe_2TiO_5 than that in TiO_2 (Fe_2O_3), which is in well accordance with the XANES and XPS results as we mentioned above. These results also suggest that in mixed oxide catalyst systems, not only in $FeTiO_x$ catalyst, the charge transfer or electron cloud deviation between different metallic atoms may be an important factor influencing their catalytic activity in certain reactions.

In addition, in order to further confirm the size of the crystallite domains of iron titanate species in $FeTiO_x$—$Ti(SO_4)_2$ catalyst, the Fe—K EXAFS and Ti—K EXAFS are calculated by FEFF8.4 code using iron titanate crystallite with different atom numbers as models. As the results shown in Fig. 7, besides of the Fe—O and Ti—O coordination peaks in the first shell, only Fe—O—Ti and Ti—O—Fe coordination
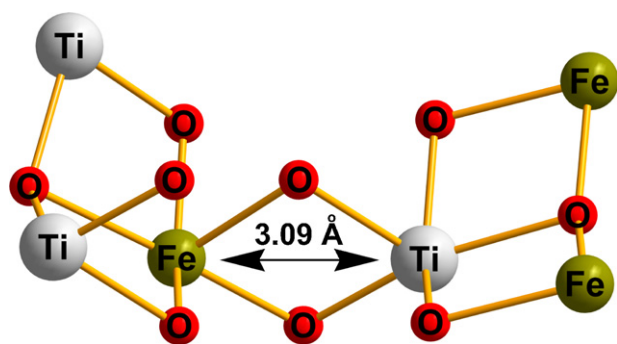
Scheme 1. Proposed model of homogeneous edge shared Fe^{3+}—$(O)_2$—Ti^{4+} structure in iron titanate catalyst derived from $Ti(SO_4)_2$ precursor.

peaks in the second shell are observed when the atom numbers in iron titanate crystallite are set to 15, which is mainly due to the inclusion of Fe^{3+}—O—Ti^{4+} linkages with edge shared oxygens in the adopted model. These results are consistent with the EXAFS data of $FeTiO_x$–$Ti(SO_4)_2$ catalyst, in which only Fe—O—Ti and Ti—O—Fe coordination peaks in the second shell are also observed. However, increasing the atom numbers further to 27 results in the appearance of another two shoulder peaks in the second coordination shells of Fe and Ti species, which is mainly due to the inclusion of Fe^{3+}—O—M and Ti^{4+}—O—M (M = Fe or Ti) linkages with corner shared oxygens. These results clearly suggest that the crystallite domains of iron titanate species in $FeTiO_x$–$Ti(SO_4)_2$ catalyst are mainly composed by *ca.* 15 atoms, which is in well agreement with the very small particle size of iron titanate crystallite that is concluded from EXAFS curve fitting results in Section 3.3.

3.5. Proposed structure of iron titanate catalyst

Based on XANES and EXAFS results, a structure model of iron titanate catalyst $FeTiO_x$–$Ti(SO_4)_2$ derived from $Ti(SO_4)_2$ precursor is proposed, as shown in Scheme 1. In this model, the edge shared Fe—O—Ti structure can be denoted as Fe^{3+}—$(O)_2$—Ti^{4+}, where Fe^{3+} and Ti^{4+} species are connected with two edge shared oxygen atoms with shorter Fe-Ti bond distance than that in well crystallized Fe_2TiO_5. This special structure is in crystallite state, *i.e.* iron titanate with very small particle size. In other words, the active phase in $FeTiO_x$–$Ti(SO_4)_2$ catalyst is macroscopically disordered but microscopically ordered. In this active phase, Fe^{3+} and Ti^{4+} species is strongly linked through edge shared fashion, and the electron density around the Fe^{3+} species is effectively reduced by the surrounding Ti^{4+} ions, which is beneficial to the enhancement of NO adsorption, oxidation ability and thus the low temperature NH_3-SCR activity. The presence of Fe^{3+}—$(O)_2$—Ti^{4+} structure in $FeTiO_x$–$Ti(SO_4)_2$ catalyst may also be responsible for its high resistance to SO_2 poisoning due to the low decomposition temperature of sulfate species on Ti^{4+}.

4. Conclusions

The micro-structure of iron titanate catalyst $FeTiO_x$–$Ti(SO_4)_2$ derived from $Ti(SO_4)_2$ precursor for NH_3-SCR of NO_x is studied in detail using XANES and EXAFS methods combined with DFT calculation. Different from the crystal structure of Fe^{3+} species in hematite Fe_2O_3 and Fe_2O_3/TiO_2 supported type catalyst, a homogeneous Fe^{3+}—$(O)_2$—Ti^{4+} structure is obviously formed in $FeTiO_x$–$Ti(SO_4)_2$ catalyst, in which the Fe^{3+} and Ti^{4+} species is strongly linked through an edge shared fashion. As confirmed by

DFT calculation, the electronic inductive effect is present between Fe^{3+} and Ti^{4+} species, which effectively reduces the electron density around the Fe^{3+}, thus leading to the enhancement of NO adsorption, oxidation ability and finally the low temperature NH_3-SCR activity. In the future study, we can stabilize this structure onto some catalyst supports with large surface areas for practical use, such as the $deNO_x$ process for flue gas in coal-fired power plants and diesel engine exhaust for environmental protection.

References

[1] H. Bosch, F. Janssen, Catalysis Today 2 (1988) 369.
[2] R.Q. Long, R.T. Yang, Journal of the American Chemical Society 121 (1999) 5595.
[3] M. Iwasaki, H. Shinjoh, Chemical Communications 47 (2011) 3966.
[4] M. Iwasaki, K. Yamazaki, K. Banno, H. Shinjoh, Journal of Catalysis 260 (2008) 205.
[5] J. Li, R. Zhu, Y. Cheng, C.K. Lambert, R.T. Yang, Environmental Science and Technology 44 (2010) 1799.
[6] J.-H. Park, H.J. Park, J.H. Baik, I.S. Nam, C.-H. Shin, J.-H. Lee, B.K. Cho, S.H. Oh, Journal of Catalysis 240 (2006) 47.
[7] A. Sultana, T. Nanba, M. Haneda, M. Sasaki, H. Hamada, Applied Catalysis B: Environment 101 (2010) 61.
[8] A. Sultana, T. Nanba, M. Sasaki, M. Haneda, K. Suzuki, H. Hamada, Catalysis Today 164 (2011) 495.
[9] G. Carja, G. Delahay, C. Signorile, B. Coq, Chemical Communications (2004) 1404.
[10] N. Apostolescu, B. Geiger, K. Hizbullah, M.T. Jan, S. Kureti, D. Reichert, F. Schott, W. Weisweiler, Applied Catalysis B: Environment 62 (2006) 104.
[11] L. Ma, J. Li, R. Ke, L. Fu, Journal of Physical Chemistry C 115 (2011) 7603.
[12] Z. Si, D. Weng, X. Wu, Y. Jiang, B. Wang, Catalysis Science & Technology 1 (2011) 453.
[13] M. Kang, E.D. Park, J.M. Kim, J.E. Yie, Catalysis Today 111 (2006) 236.
[14] P.G. Smirniotis, D.A. Peña, B.S. Uphade, Angewandte Chemie International Edition 40 (2001) 2479.
[15] X. Tang, J. Hao, W. Xu, J. Li, Catalysis Communications 8 (2007) 329.
[16] Z. Wu, B. Jiang, Y. Liu, H. Wang, R. Jin, Environmental Science and Technology 41 (2007) 5812.
[17] A. Sultana, M., Sasaki, H., Hamada, Catalysis Today doi:10.1016/j.cattod.2011.09.018.
[18] S. Yang, C. Wang, J. Li, N. Yan, L. Ma, H. Chang, Applied Catalysis B: Environment 110 (2011) 71.
[19] Y. Li, H. Cheng, D. Li, Y. Qin, Y. Xie, S. Wang, Chemical Communications (2008) 1470.
[20] Z. Si, D. Weng, X. Wu, R. Ran, Z. Ma, Catalysis Communications 17 (2012) 146.
[21] J. Li, H. Chang, L. Ma, J. Hao, R.T. Yang, Catalysis Today 175 (2011) 147.
[22] G. Cavataio, J. Girard, J.E. Patterson, C. Montreuil, Y. Cheng, C.K. Lambert, SAE Technical Paper (2007) 01–1575.
[23] F. Liu, H. He, C. Zhang, Chemical Communications (2008) 2043.
[24] F. Liu, H. He, C. Zhang, Z. Feng, L. Zheng, Y. Xie, T. Hu, Applied Catalysis B: Environment 96 (2010) 408.
[25] F. Liu, H. He, Journal of Physical Chemistry C 114 (2010) 16929.
[26] F. Liu, K. Asakura, H. He, Y. Liu, W. Shan, X. Shi, C. Zhang, Catalysis Today 164 (2011) 488.
[27] J.W. Cook, D.E. Sayers, Journal of Applied Physics 52 (1981) 5024.
[28] A.L. Ankudinov, B. Ravel, J.J. Rehr, S.D. Conradson, Physical Review B 58 (1998) 7565.
[29] B. Delley, Journal of Chemical Physics 92 (1990) 508.
[30] B. Delley, Journal of Chemical Physics 113 (2000) 7756.
[31] S. Yamazaki, N. Fujinaga, K. Araki, Applied Catalysis A 210 (2001) 97.
[32] F. Liu, K. Asakura, H. He, W. Shan, X. Shi, C. Zhang, Applied Catalysis B 103 (2011) 369.
[33] F. Liu, H. He, C. Zhang, W. Shan, X. Shi, Catalysis Today 175 (2011) 18.
[34] R.Q. Long, R.T. Yang, Journal of Catalysis 186 (1999) 254.
[35] A. Kato, S. Matsuda, F. Nakajima, M. Imanari, Y. Watanabe, Journal of Physical Chemistry 85 (1981) 1710.